nature physics

Article

https://doi.org/10.1038/s41567-025-03165-4

Geometric origin of particle and dislocation dynamics during grain boundary migration

Received: 7 September 2024

Accepted: 18 December 2025

Published online: 9 March 2026

Check for updates

Berend van der Meer[1,2,3], Mathieu G. Baltussen[1,2,4], François A. Lavergne[2], Arran Curran[1,2], Marjolein Dijkstra[4] & Roel P. A. Dullens[1,2]

Grain boundaries are complex defects in polycrystalline systems and their migration has a key role in determining the properties of such solids. Understanding grain boundary motion in terms of both particle and dislocation dynamics remains a central problem. Here we establish a fundamental geometric principle governing grain boundary migration at the microscopic level: particles preferentially transition between grains at specific lattice equivalence points identified through a refined O-lattice construction. We validate this principle using loop-shaped grain boundaries in two-dimensional colloidal crystals created with holographic optical tweezers and computer simulations. Building on this principle, we develop a geometric framework that accurately predicts the microscopic dynamics of both particles and dislocations during grain boundary migration. Our results shed light on the microscopic mechanism of grain boundary migration and reveal the intrinsic connection between the dynamics of particles and dislocations.

Grain boundary (GB) migration induces substantial structural changes in polycrystalline solids such as ceramics, rocks and metals, and it has a pronounced effect on the macroscopic properties of these materials[1–3]. At the atomic scale, GB migration is a complex process involving the coordinated movement of atoms between lattice sites of neighbouring grains. Recent work on atomic GBs using high-resolution electron microscopy has shown that the displacement of atoms from one grain to another is closely related to the arrangement of the atoms within the GB itself[4,5]. Indeed, GBs are not simply amorphous structures. They have been described in various ways, including combinations of different structural units[6], coincidence site lattices[7] and dislocations[8]. However, predicting how the GB structure influences its migration is challenging owing to the dynamic nature of the GB structure, which evolves as the boundary migrates[4,5,9,10].

GB migration also involves the interaction and motion of defects, such as dislocations and disconnections[11–16], which are confined to the GB plane and are subject to topological constraints imposed by the surrounding crystalline structure[17]. Various models have been proposed to describe GB migration, including the Cahn model[18,19], which is based on dislocation motion, the pure shuffling model for high-angle GBs[20] and the disconnection model[11,12,21,22]. While these established models have profoundly shaped our understanding of GB evolution and the role of defects, they typically focus on specific mechanisms—such as dislocation glide, disconnection motion or defect-mediated coupling—rather than providing a fully microscopic, predictive framework that captures the simultaneous dynamics of individual particles and defects. Consequently, despite substantial efforts to characterize the microscopic mechanism for GB motion (see, for example, refs. 4,9,15,16,19,23,24), a comprehensive understanding of the dynamics of both atoms and defects during the GB migration process remains largely unclear.

From an experimental standpoint, systems composed of micrometre-sized colloidal spheres are widely accepted as an ideal platform for studying condensed-matter phenomena at the particle level using microscopy (see, for example, refs. 25–33). More recently, colloidal crystals have also emerged as a convenient toolkit for investigating GB behaviour[34–41], with the key advantage that these systems can be readily manipulated using optical forces[37–41]. This allows for the creation of well-defined model GB structures, where key parameters

[1]Institute for Molecules and Materials, Radboud University, Nijmegen, The Netherlands. [2]Department of Chemistry, Physical and Theoretical Chemistry Laboratory, University of Oxford, Oxford, UK. [3]Physical Chemistry and Soft Matter, Wageningen University & Research, Wageningen, The Netherlands. [4]Soft Condensed Matter, Debye Institute for Nanomaterials Science, Utrecht University, Utrecht, The Netherlands. e-mail: roel.dullens@ru.nl

such as the difference in orientation between neighbouring crystal domains (misorientation) and the GB curvature can be precisely controlled[39]. As both individual particles and dislocations can be directly visualized and tracked in colloidal crystals[30,37,39], they are ideal model systems for uncovering the mechanisms underlying GB migration.

In this work, we establish a fundamental and purely geometric principle that governs the microscopic dynamics of particles and dislocations during GB migration. This principle states that particles preferentially transition between grains at specific lattice equivalence points, which are identified through a refined O-lattice construction and depend solely on the relative orientation of the two crystals. By experimentally investigating loop-shaped GBs in a two-dimensional colloidal model system and through computer simulations, we demonstrate how this principle enables a geometric framework that accurately predicts the particle-level displacements during GB migration. Moreover, this same geometric framework allows us to predict the precise locations and orientations of dislocations within GBs and describe their observed motion during GB migration. Crucially, our framework not only describes the intricate dynamics of both particles and dislocations but also establishes a direct link between them by identifying their common geometric origin. This enables a comprehensive understanding of the microscopic dynamics underlying GB migration within a unified theoretical framework. In principle, our framework can be applied to any material, as it relies solely on the difference in orientation between two crystals, a purely geometric property that is independent of whether the material is atomic, molecular or colloidal.

Results and discussion

Particle and dislocation dynamics during GB migration

We investigate the microscopic dynamics of GB motion by focusing on arguably the simplest GB geometry: a loop-shaped GB within a two-dimensional host crystal. Starting with a crystalline monolayer of nearly hard-sphere colloidal particles[42] (Methods), we create a loop-shaped GB by using an optical vortex to rotate a circular patch within a large host crystal domain[39]. This rotation continues until the desired misorientation is achieved, after which we deactivate the optical tweezer and study the curvature-driven GB migration[43,44] free from external forces.

First, we examine a loop-shaped GB with a misorientation of $\theta \approx 13°$. A false-coloured microscopy image of the loop-shaped GB is shown in Fig. 1a,b, where particles are colour-coded according to their local orientation[39]. For this particular misorientation, a finite fraction of lattice sites coincide between the rotated and host lattices. These sites form the coincident site lattice (CSL; white circles in Fig. 1b) with a lattice spacing substantially larger than the interparticle spacing: $a_{\mathrm{CSL}} = a\sqrt{\Sigma}$, where Σ (= 19) denotes the reciprocal density of coincidence sites[7,45].

To examine the particle-level dynamics underlying the motion of this GB, commonly denoted as a Σ19 boundary, we colour-code the particle trajectories according to the elapsed time for a region that is initially located within the rotated grain (Fig. 1c). As the GB migrates (from right to left in this particular region), particles are displaced from their initial sites in the rotated grain to their final sites in the host grain, thereby adopting the orientation of the host crystal. During this process, most particles show noticeable displacements, while the particles located at the sites of the CSL (black circles) remain virtually in place as their positions are compatible with both crystals. Importantly, the particles at CSL sites thus adopt a new crystal orientation via a collective block rotation of their nearest neighbours around them (Fig. 1d), but without moving. A similar collective block rotation is observed for the second shell of nearest neighbours, but it involves larger displacements as they are farther away from the centre of rotation. These local block rotations of particles around CSL sites lead to the characteristic hexagonal cell-like structure seen in the particle trajectories (Fig. 1c). Notably, the behaviour observed in our experiments is reminiscent of the ordered patterns of particle displacement observed in colloidal crystals[41] and computer simulations of three-dimensional systems[23,24,46–48].

Next, we characterize the dislocation dynamics during GB migration. We visualize the trajectories of the dislocations by plotting each dislocation as a solid connection between the seven- and fivefold coordinated particles, colour-coding them according to time (Fig. 1e). Strikingly, the dislocation trajectories shown in Fig. 1f reveal the same characteristic hexagonal cell-like structure seen in the particle trajectories. The paths taken by the dislocations correspond to the regions of largest particle displacement. The local block rotations observed in the particle dynamics are therefore directly linked to the reaction and 'glide' of dislocations along these paths, which are also where the mismatch between the rotated and host lattice is greatest. Clearly, this strong correlation between the particle and dislocation dynamics arises from the fact that the particle rearrangements involved in GB migration are strongly constrained by the fact that dislocation 'glide' can only occur along the Burgers vector[49].

To test the generality of these particle-level GB migration mechanisms, we now examine the particle trajectories for various misorientations (Fig. 1g–j), including cases that do not correspond to a CSL (Fig. 1j). Intriguingly, in all cases, distinct hexagonal cellular patterns are observed, and the size and complexity of each 'cell' is determined by the misorientation. Importantly, we consistently observe that particles at the centre of the cells remain largely stationary, while those at the edges undergo larger displacements (Fig. 1g–j), irrespective of whether the misorientation corresponds to a CSL or not. This suggests that these cellular patterns and the associated particle dynamics are a general phenomenon in GB migration and not solely restricted to CSL boundaries.

To understand the origin of these regions of high and low particle displacement underlying GB migration for any misorientations, including cases where no CSL is present, we use O-lattice theory[50], which is a generalization of the CSL theory for arbitrary misorientations. The O-lattice theory has been successfully used to describe the static structure of GBs (see, for example, refs. 51–55) by identifying regions of good and poor fit between the two crystal lattices. The main difference between the CSL and O-lattice approaches lies in the nature of the coincidences they consider. While the CSL method restricts coincident points to lattice points exclusively, the O-lattice approach broadens the definition of coincidence to encompass any point within the crystal unit cell, provided that the internal coordinates of these points are equivalent in the unit cells of both lattices[50]. As a result, these so-called O-lattice equivalence points do not necessarily have to correspond to lattice points. To construct the O-lattice, one considers two lattices $\mathbf{T}_1$ and $\mathbf{T}_2$, which are related via a simple rotation over the misorientation angle θ:

$$\mathbf{T}_2 = A(\theta)\mathbf{T}_1, \tag{1}$$

with $A(\theta)$ the corresponding transformation matrix. Next, the lattice of equivalence points $\mathbf{r}_{\mathrm{O}}$, the so-called O-lattice, is determined by[50]:

$$\mathbf{r}_{\mathrm{O}} = [I - A^{-1}(\theta)]^{-1}\mathbf{T}_1, \tag{2}$$

where I is the identity matrix. Note that for misorientations corresponding to a CSL, the points of the O-lattice $\mathbf{r}_{\mathrm{O}}$—or a subset thereof—constitute the CSL. In Fig. 1g–i, we plot these CSLs and their corresponding Voronoi cells as obtained from the O-lattice on top of our trajectories (markers). These cells capture the hexagonal cell-like structure of the particle dynamics very well.

Crucially, the same O-lattice construction can now also be used for non-CSL misorientations (Fig. 1j), which, intriguingly, reveals a very similar cell-like pattern to the CSL misorientations. Near the O-lattice

https://doi.org/10.1038/s41567-025-03165-4

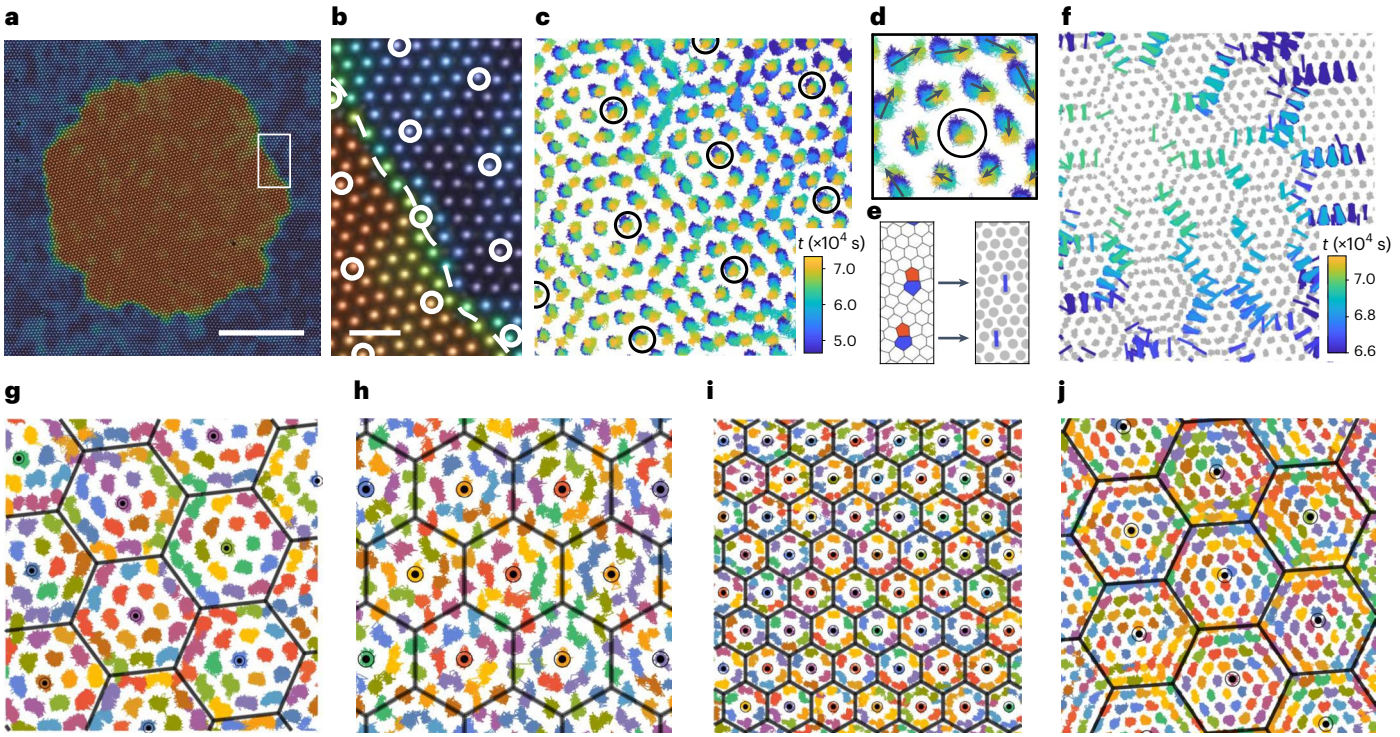

Fig. 1 | Experimental observation of particle and dislocation dynamics underlying the migration of loop-shaped GBs in a two-dimensional colloidal crystal. a, False-coloured microscopy image of a loop-shaped GB with a misorientation $\theta \approx 13°$. Scale bar, 80 µm. **b**, A close-up of part (white box in **a**) of the GB (dashed white line) with CSL sites superimposed (white markers). Scale bar, 8 µm. **c**, Particle trajectories colour-coded according to the elapsed time, revealing collective block rotations around CSL sites (black circles) as the GB migrates from right to left. A stationary central particle is located on each CSL site. **d**, A close-up showing the collective block rotation around a single CSL site. **e**, Example of a Voronoi construction of a section of the GB, showing dislocations characterized by pairs of seven- and fivefold coordinated particles, shown in blue and red, respectively (left). The position and orientation of these dislocations can be conveniently visualized by plotting each dislocation as a solid connection between the seven- and fivefold defects (right). **f**, Dislocation trajectories colour-coded by time with particle positions superimposed (grey), showing how local block rotations observed in the particle dynamics correspond to the reaction and glide of dislocations along pathways where particle displacements are most pronounced. **g**–**j**, Particle trajectories for a wide range of misorientations, showing distinct unit cells of particle displacement around a central stationary particle. Each colour represents an individual particle. **g**–**i**, For misorientations close to a CSL, the positions of the stationary particles align with the CSL (markers). Misorientations and corresponding CSL: $\theta \approx 13°$, $\Sigma 19$ (**g**), $\theta \approx 28°$, $\Sigma 13$ (**h**) $\theta \approx 22°$, $\Sigma 7$ (**i**). **j**, The same behaviour is observed when no CSL is present, but now the positions of the stationary particles are given by the O-lattice (markers). Misorientation: $\theta \approx 9°$.

points (markers), particles are largely stationary, whereas near the edges of the hexagonal cells, the particles move substantially more, similar to the CSL cases. While both the CSL- and O-lattice frameworks offer a global description of the particle dynamics in terms of regions of high and low correspondence between the two lattices, they do not provide a detailed microscopic description of the particle-level displacements underlying the lattice transformation during GB migration.

GB transition points

To develop a purely geometric framework that predicts the particle-level displacements underlying the migration of a GB with an arbitrary misorientation, we adapt O-lattice theory to uniquely identify a set of equivalence points between both lattices that act as transition points for particles displacing between grains. Importantly, owing to the six-fold symmetry of the hexagonal lattice, the transformation matrix is not uniquely defined: rotations of $\varphi = \theta + w \times 60°$ with $w = [0 \ldots 5]$ all give the same GB misorientation θ yet result in large differences in the obtained O-lattice. Therefore, we now generate the O-lattice using φ instead of θ:

$$\mathbf{r}_O = [I - A^{-1}(\varphi)]^{-1}\mathbf{T}_1. \quad (3)$$

This difference is illustrated in Fig. 2a,b for a misorientation of $\theta = 20°$, where it is clearly observed that the O-lattice for $w = 0$ (Fig. 2a) has a much larger spacing than the one for $w = 3$ (Fig. 2b). As the O-lattice points $\mathbf{r}_O$ have the same internal coordinates in both lattices[50], we postulate that they may act as transition points for particles switching grain.

To identify which O-lattice, that is which value of w, might contain O-lattice points capable of serving as transition points, we hypothesize that these transition points must be positioned in close proximity to the lattice points of both crystals. To this end, we calculate for all w the mean distance between a lattice site $\mathbf{T}_{1,i}$ and its nearest O-lattice site $\mathbf{r}_{O,j}$ using $\langle|\Delta\mathbf{R}_{T,O}|\rangle = \langle|\mathbf{T}_{1,i} - \mathbf{r}_{O,j}|\rangle$, as shown in Fig. 2d. Here, the indices i and j refer to site i of lattice $\mathbf{T}_1$ and the nearest point j in the O-lattice $\mathbf{r}_O$. Using this criterion we find that the O-lattice with $w = 3$ yields the lowest value of $\langle|\Delta\mathbf{R}_{T,O}|\rangle$ for all possible GB misorientations θ. Hence, we anticipate the O-lattice for $w = 3$ to provide the most efficient way for particles to transition between the two crystal lattices. This transition process is illustrated in Fig. 2c, which shows how two O-lattice points act as transition points for particles displacing between the two lattices, as indicated by the black arrows. Note that $w = 3$ also corresponds to the smallest O-lattice spacing (Extended Data Fig. 1b). Our interpretation of this O-lattice as a predictor of dynamic transition points is an important conceptual and practical departure from conventional O-lattice theory[50], which primarily focuses on the structural analysis of GBs[51–55] and the importance of the O-lattice with the largest unit cells. In contrast, we refine the framework of O-lattice theory to identify a set of equivalence points between the two lattices that serve as dynamic transition points—locations where particles transfer between grains during GB migration. For clarity, when

https://doi.org/10.1038/s41567-025-03165-4

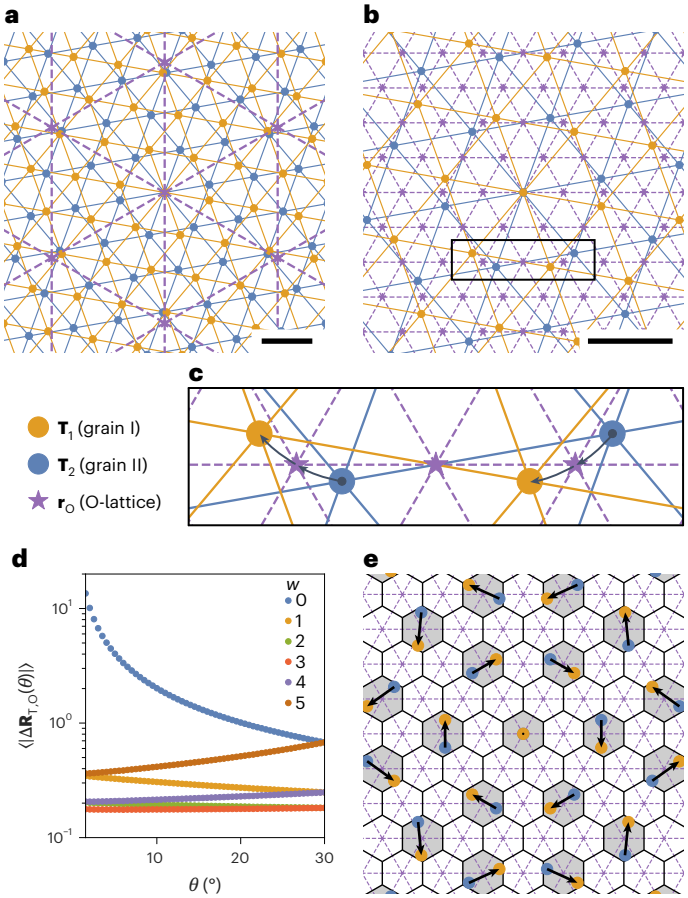

Fig. 2 | Identifying GB transition points through O-lattice construction. **a**,**b**, Bicrystallographic pattern (orange and blue lattice) with superimposed O-lattice construction (purple). The blue and orange lattices are rotated relative to each other by $\varphi = 20°$ ($w = 0$; **a**) and by $\varphi = 200°$ ($w = 3$; **b**). Both rotations result in the same misorientation $\theta = 20°$, yet give rise to vastly different O-lattices. Note the difference in scale between **a** and **b**, as denoted by the scale bar, which is equal to the lattice spacing of the orange and blue crystals. **c**, Close-up view illustrating how particles from the blue lattice can transition to the orange lattice via an intermediate O-lattice point, which acts as a GB transition point. **d**, The calculated average distance between a lattice site and its nearest O-lattice site $\langle|\Delta\mathbf{R}_{T,O}|\rangle$, as a function of the misorientation θ for all values of w. **e**, O-lattice cell construction for $w = 3$, showing two types of cell: 'empty' O-cells, which contain no lattice points, and 'filled' O-cells (shaded), which contain a single lattice point from both crystals. These filled O-cells represent the regions within which particles are expected to transition from the blue to the orange crystal lattice by displacing according to the black arrows.

we refer to 'our' O-lattice construction or 'our' geometric approach throughout this work, we exclusively refer to this dynamic reinterpretation based on the O-lattice with the smallest lattice spacing.

Figure 2e illustrates how the transition points may be identified from the O-lattice with the smallest spacing ($w = 3$), where the O-lattice is shown in purple and the 2 crystal lattices in blue and orange for a misorientation $\theta = 20°$. Clearly, the lattice sites of the blue and orange crystals always pair up near a subset of O-lattice points, whereas other O-lattice points have no lattice sites nearby. This is visualized more clearly by performing a Voronoi construction on the O-lattice (Fig. 2e)—referred to as the 'O-cell construction'—which reveals two types of O-lattice cell: 'filled' O-cells containing a single lattice site from both crystals (shaded cells) and 'empty' O-cells containing no lattice sites (white cells). We thus expect that only the O-lattice points of the filled O-cells act as transition points for particles displacing between the two lattice sites in the cell. Conversely, no particle rearrangements are expected to occur within empty O-cells. Hence, both filled and empty O-cells are crucial to understanding the particle dynamics underlying GB motion.

O-lattice prediction of particle dynamics

To compare the experimental particle trajectories with our geometrical O-lattice predictions, we generate predicted displacement vectors by connecting the two lattice sites within a single 'filled' O-cell. The geometric framework inherently treats both crystal lattices equivalently, providing predictions for particle transitions in either direction. However, owing to the loop-shaped geometry of our GB, the curvature-driven shrinkage results in an inwards migration of the GB. Consequently, the predicted displacement vectors specifically describe particles transitioning from the rotated lattice to the host lattice. In contrast, particles within the host domain fluctuate around their lattice positions throughout this process, as they are not affected by the inwards-moving GB. The origin of the predicted displacement map was chosen such that it achieves the best match with the measured trajectories (Methods). We plot the predicted particle displacements (black arrows) on top of the experimental particle trajectories for a wide range of θ, covering both non-CSL (Fig. 3a,b) and CSL cases (Extended Data Fig. 2c–e). We find excellent agreement between the predicted and observed particle displacements, demonstrating that our geometric O-lattice framework accurately captures how the transition points govern the complex particle dynamics during GB migration. Remarkably, the agreement even holds for GB misorientations with complex particle displacement patterns (see, for example, Fig. 3b), highlighting the general applicability of our geometric approach.

Inherent to the thermal nature of our system, we anticipate that particle displacements may not always precisely conform to the predictions of our geometric framework. To systematically investigate this aspect, we perform dynamic Monte Carlo (dMC) simulations[56] of hard spheres (Methods) across a range of packing fractions ϕ, which in a hard-sphere system controls the importance of thermal fluctuations relative to the crystal's elastic constants. We quantify the agreement between predicted and observed particle displacements for our simulated GB loops by monitoring the fraction $P = N_p/N$ of particles that displace between lattice sites as predicted by our O-cell construction, where N_p represents the number of particles displacing as predicted and N is the total number of displacing particles (Methods). The fraction of particles that displace as predicted increases with packing fraction ϕ (dashed lines in Fig. 3c) for all misorientations considered, indicating that thermal fluctuations significantly contribute to the stochasticity in the particle dynamics as ϕ decreases. Therefore, at low ϕ, the particle dynamics is primarily 'geometry guided', while at high ϕ it becomes 'geometry determined' (see also Extended Data Fig. 3).

Our geometric O-lattice framework assumes a fixed misorientation and therefore does not account for changes in misorientation over time. However, grain rotation is commonly observed in loop-shaped GBs[39,40,57,58], driven by mechanisms such as coupled GB migration or GB sliding[18,19]. For example, a GB loop starting with $\theta = 9°$ shows a significant increase in misorientation during its shrinkage, consistent with coupled GB migration (Extended Data Fig. 5a). As this rotation proceeds, the growing discrepancy between the initial misorientation (assumed by our model) and the actual evolving misorientation reduces the accuracy of our predictions, resulting in a lower value of P. To demonstrate that our approach can indeed fully predict the particle dynamics in the absence of grain rotation, we again perform dMC simulations, but now with a fixed misorientation using an external biasing potential (Methods). Under these conditions, and at sufficiently high packing fractions ϕ, nearly all particles ($P \approx 1$) follow the predicted displacements (solid lines in Fig. 3c). This confirms the validity of our geometric model and shows that deviations from the predictions arise primarily owing to either thermal fluctuations or grain rotation.

https://doi.org/10.1038/s41567-025-03165-4

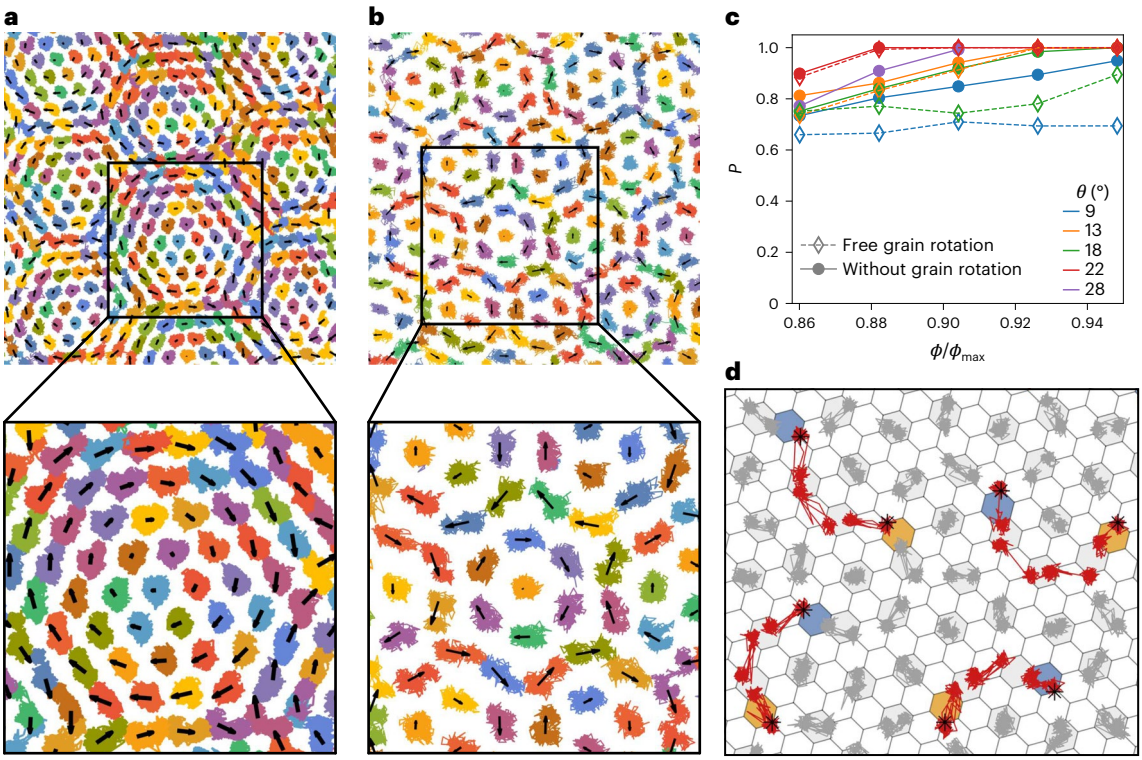

Fig. 3 | Predicting the particle dynamics underlying GB migration through O-cell construction. a,**b**, Experimentally observed particle trajectories with superimposed particle displacements as predicted by our O-cell approach (black arrows) for $\theta = 9°$ (**a**) and $\theta = 18°$ (**b**). **c**, The fraction of particles P that displace as predicted as a function of the packing fractions ϕ in dMC simulations. At low ϕ, a significant fraction of particles does not displace as predicted owing to pronounced thermal fluctuations. However, at high ϕ, such thermal effects become negligible and the particle dynamics becomes highly predictable $P \approx 1$. Open markers correspond to simulations where grain rotation was allowed to occur freely and closed markers correspond to simulations in which the misorientation was fixed using an external biasing potential. The error bars for each state point ($N = 4$) are on the order of the symbol size or smaller and are omitted to retain a clear presentation of the data. **d**, O-cell construction featuring 'incoherent' O-cells with superimposed trajectories as measured in dMC simulations, for a fixed misorientation $\theta = 29°$. A string of particle displacements (red trajectories) originates from each 'incoherent' cell containing a lattice site of the rotated grain (blue cells) and terminates at an 'incoherent' cell containing a lattice site of the host grain (orange cells).

Owing to its fully geometric nature, our general framework is expected to be applicable to systems with a diverse range of interaction types. To test whether our predictions are robust against such changes in interparticle interaction, we perform dMC simulations for three other interaction potentials. Specifically, we consider systems composed of: (1) Weeks–Chandler–Andersen particles modelling short-ranged, yet continuous, repulsive interactions (Extended Data Fig. 6a1); (2) Yukawa particles exhibiting substantially longer-ranged soft repulsive interactions[59] (Extended Data Fig. 6b1); and (3) Lennard–Jones particles with attractive interactions (Extended Data Fig. 6c1). A more detailed description of these three systems can be found in Methods. Across all three systems, we compare the observed particle trajectories with the predicted displacement maps and find consistently good agreement (Extended Data Fig. 6a2–c2), similar to that observed in the hard-sphere case. To quantify this agreement, we again compute the fraction of particles P that follow the predicted displacements. For each interaction type, we observe a clear crossover from a 'geometry guided' regime—where thermal fluctuations obscure the underlying geometric preference—to a 'geometry determined' regime at higher particle number densities, where such thermal effects are diminished (Extended Data Fig. 6a3–c3). However, reaching this geometry-determined limit is more challenging in systems with softer and/or attractive interactions (Extended Data Fig. 6b3,c3). This may be attributed to the interparticle forces modifying the GB structure and thereby altering the local rearrangement pathways[4,5]. Alternatively, it is plausible that the particle number densities explored in our simulations are simply not high enough to sufficiently suppress thermal effects. Unfortunately, further increasing the particle number density (or lowering the temperature) considerably slows down the kinetics of GB shrinkage, which limits our ability to access the dynamics at these state points. The relatively easy attainment of the 'geometry determined' limit in hard spheres is to be expected, given that the behaviour of hard particles is governed entirely by geometric constraints.

Intriguingly, for some misorientations, our O-cell construction also predicts the existence of a third type of O-cell, which contains only a single lattice point from one of the two crystals and therefore demarcates an incoherence between the two crystals. Consequently, when a particle in an 'incoherent' O-cell displaces, it triggers a string of displacements that ultimately reaches another incoherent O-cell containing a single lattice point from the opposite crystal, completing the grain transition for all particles in the rearrangement string. To specifically target the misorientations where 'incoherent' O-cells occur, we use dMC simulations in which the misorientation is kept constant (Methods), also because our experiments are conducted in the 'geometry guided' regime where the particle dynamics is affected by thermal fluctuations. In our simulations, we indeed observe that incoherent O-cells lead to a remarkably rich dynamics during grain transition, as is evident from plotting the particle trajectories on top of the O-cell construction (Fig. 3d). Here, a string of particle displacements (red trajectories) originates from an 'incoherent' cell containing a lattice site of the rotated grain (blue cell) and ends at an 'incoherent' cell containing a lattice site of the host grain (orange cell). Our framework thus also provides the geometric underpinning for the origin of this string-like motion and accurately predicts

https://doi.org/10.1038/s41567-025-03165-4

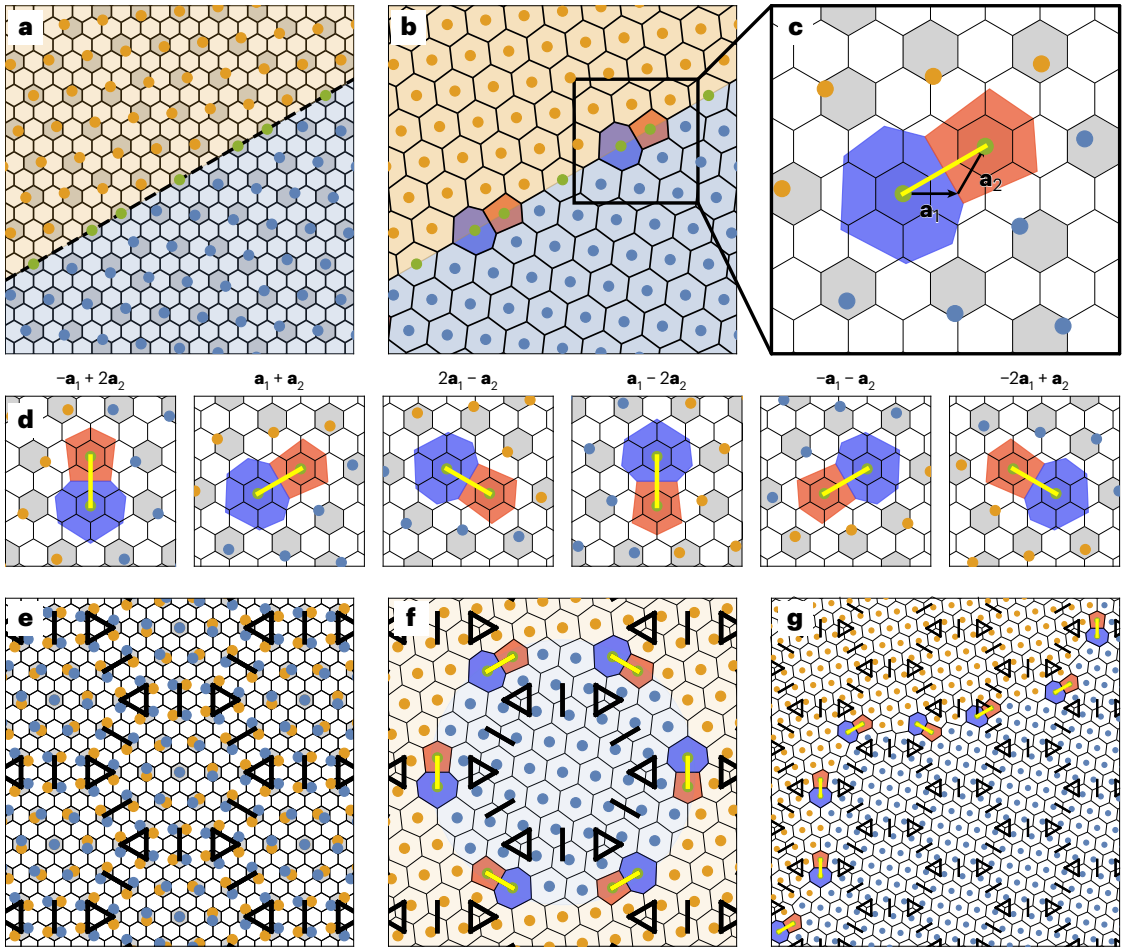

Fig. 4 | Predicting GB dislocation structure through O-cell construction. Note that in this figure, we use an example misorientation of $\theta = 13.2°$. **a**, Using the O-cell construction method, we generate a GB (dashed line) that separates two crystal domains. To achieve this, particles are placed on lattice sites of the orange crystal for O-cells situated above the GB line, while for O-cells below the GB line, particles are placed on lattice sites of the blue crystal. For O-cells located on the GB line, particles are instead placed on the O-lattice point (green). **b**, Using Voronoi construction on the obtained particle configuration, dislocations are easily identified within this GB as pairs of 7–5 defects. **c**, In a detailed view of a dislocation, overlaid with O-cell construction, it becomes evident that the 7–5 connector of the dislocation is given by a combination of lattice vectors of the O-lattice. **d**, The six elementary GB dislocations, which all arise as simple combinations of lattice vectors of the O-lattice. **e**, O-cell construction with superimposed a map of all positions where dislocations can potentially be present. Here each dislocation site is plotted as a black line with its orientation representing the line that connects the 7 and 5 defects. **f**, Example of a loop-shaped GB constructed using this dislocation mapping. By selecting a circular path of dislocation sites (lines highlighted in yellow) and placing particles inside (outside) this loop on lattice sites of the blue (orange) crystal, a loop-shaped GB containing all six elementary dislocation orientations emerges. **g**, Likewise, a curved planar GB may be constructed by selecting a different path of dislocation sites (highlighted in yellow).

the locations of 'incoherent' O-cells that act as sources and sinks for this type of motion. Intriguingly, such string-like motion has previously been characterized as glassy behaviour[35,60], also in light of the somewhat amorphous nature of GBs. While it is true that significant thermal fluctuations can induce this anomalous behaviour, particularly linked to the decreasing P in Fig. 3c, our findings also demonstrate that this dynamics can, in fact, have a more fundamental geometric origin.

O-lattice prediction of dislocation dynamics

Lastly, we demonstrate how our geometric O-cell construction also describes the GB dislocation structure and its evolution during GB motion. To demonstrate this, we first clarify how dislocations may be identified from our O-lattice construction. To this end, we create a system composed of two grains using the following procedure. Starting with a host and rotated crystal, we generate an O-cell construction, revealing all 'filled' O-cells (shaded cells in Fig. 4a). Within each filled O-cell, the particle sits on either one of the lattice sites or on the transition point between them, that is the O-lattice point (Fig. 2c). To obtain the two-grain system shown in Fig. 4a, we place the particles within the filled O-cells as follows: the particles in the upper grain (orange area) are placed on lattice sites of the orange host crystal, and the particles in the lower grain (blue area) occupy sites of the blue rotated crystal. Given the transitional nature of particles at the GB, we place these boundary particles at the O-lattice points.

Once the two-grain system is created, we determine the number of nearest neighbours for each particle using a Voronoi construction on the particle positions. The dislocations are then identified as pairs of 7–5 defects, as depicted in Fig. 4b. Remarkably, a closer examination of the relation between the dislocations and the O-lattice (Fig. 4c) reveals that the 7–5 connector of the dislocation is in fact given by a combination of lattice vectors of the O-lattice $\mathbf{a}_1$ and $\mathbf{a}_2$. This relationship is robust to changes in misorientation θ, thus establishing a direct connection between our O-lattice construction and GB dislocations. Considering the six-fold symmetry of our lattice, the six elementary dislocations[39] that represent all possible GB dislocation orientations can be identified as combinations of the O-lattice vectors, $\mathbf{a}_1$ and $\mathbf{a}_2$, as shown in Fig. 4d.

https://doi.org/10.1038/s41567-025-03165-4

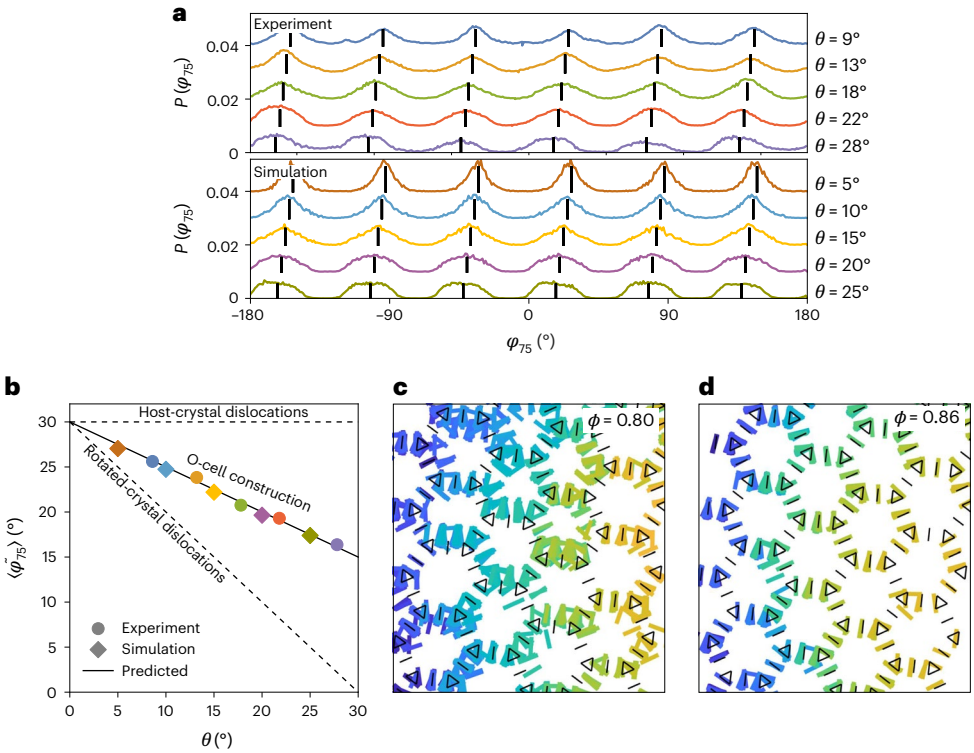

Fig. 5 | Comparing the dislocation orientations and positions predicted by our O-cell approach with those observed in experiments and dMC simulations. **a**, The probability distribution function $P(\varphi_{75})$ of the dislocation orientations relative to the host crystal axis as observed in experiments (top) and dMC simulations (bottom). To aid in visualization, histograms for different misorientations θ have been vertically offset. The vertical black lines represent the dislocation orientations predicted by our geometric O-cell construction. **b**, The mean dislocation orientation $\langle\tilde{\varphi}_{75}\rangle$ upon accounting for six-fold symmetry, as measured in experiments (circles) and dMC simulations (diamonds) for a wide range of misorientations θ. The measured dislocation orientations are in excellent agreement with the predictions from our O-cell construction. Dashed lines correspond to the mean dislocation orientation typical of dislocations found within the bulk of either crystal lattice. **c**,**d**, Dislocation trajectories with superimposed map of potential dislocation sites as predicted by our O-cell construction for dMC simulations at $\phi = 0.80$ (**c**) and $\phi = 0.86$ (**d**). Colour indicates time, with blue representing early times and yellow representing late times.

An important consequence of these GB dislocations occurring as exact combinations of O-lattice vectors is that their appearance is restricted to locations where two filled O-cells are separated by one of these exact combinations of $\mathbf{a}_1$ and $\mathbf{a}_2$. This allows us to establish a comprehensive map of all possible positions where such GB dislocations can occur. An example of such a map is shown in Fig. 4e for a misorientation of $\theta = 13.2°$. Here, each potential dislocation site and its orientation is represented by the solid black line that connects the constituting seven- and fivefold defects. Importantly, which of these sites actually have dislocations depends on the shape and position of the GB. In fact, using this map of possible dislocation sites, a GB of any desired shape can be formed by choosing a path of dislocation sites. This is illustrated in Fig. 4f, where we selected a loop-shaped path (yellow lines) from all possible dislocation sites (black lines). A loop-shaped GB then results by placing particles at these GB dislocations at their O-lattice point, while all other particles are placed at a lattice site corresponding to their respective crystals. Likewise, a curved planar GB may similarly be constructed by selecting a different path of dislocation sites (Fig. 4g).

Next, we compare the predicted dislocation orientations, as given by the six elementary GB dislocations (Fig. 4d), with those observed in both our experiments and dMC simulations. To this end, we quantify the orientation of a dislocation by measuring the angle φ_{75} formed by the 7–5 connector relative to the host crystal axis. The probability distribution function of the dislocation orientations $P(\varphi_{75})$ as measured in experiments and simulations are shown in Fig. 5a, together with our O-lattice predictions of the dislocation orientations (solid sticks) for a range of misorientations θ. It is readily apparent that the prominent peaks in the distribution $P(\varphi_{75})$ observed in our measurements align perfectly with the predicted dislocation orientations. Note that as the misorientation θ increases, the peaks of $P(\varphi_{75})$ shift to lower values, by an amount in line with the predictions.

We further highlight the excellent agreement between the measured and predicted dislocation orientations by introducing a mean dislocation orientation that accounts for the hexagonal symmetry of the lattice, which we denote as $\langle\tilde{\varphi}_{75}\rangle = \langle\varphi_{75} \bmod \pi/3\rangle$. In Fig. 5b, we plot $\langle\tilde{\varphi}_{75}\rangle$ for a wide range of misorientations θ, demonstrating that the predicted mean dislocation orientation based on our O-cell construction (solid line) closely matches the mean dislocation orientation as measured in experiments and simulations (markers). It is worth emphasizing again that these GB dislocations are not associated with either crystal lattice but are, in fact, related to the O-lattice itself. Namely, the orientations of these GB dislocations differ from the orientations typical of dislocations found within the bulk of either crystal lattice, as indicated by the dashed lines in Fig. 5b.

Finally, we show how our O-cell construction also predicts the evolution of the dislocation structure during GB migration. In Fig. 5c,d, we plot the dislocation trajectories as measured in dMC simulations (coloured lines) on top of the map containing all possible dislocation positions (black lines). Clearly, the dislocations glide and react along the pathways indicated by the predictions based on our O-lattice construction. Strikingly, the dislocation map based on our geometric O-lattice approach effectively provides a roadmap for the transport of dislocations during GB migration. Similarly to the particle dynamics, the dislocation dynamics—in terms of both motion and reactions—are

essentially fully dictated by the underlying geometry, especially as the packing fraction ϕ increases (Fig. 5d). Crucially, as the microscopic dynamics of both particles and dislocations are captured by the same geometric construction, our O-cell approach thus provides a unified geometric framework for the microscopic mechanism underlying GB migration.

Conclusion

We have established a fundamental geometric principle that underlies the microscopic mechanism of GB migration: the presence of lattice equivalence points that act as transition points for particles changing grain. This principle enables accurate prediction of the intricate dynamics of particles and dislocations during GB migration. The geometric framework we developed not only accurately predicts the microscopic dynamics of both particles and dislocations during GB motion but also demonstrates the intrinsic connection between these dynamics. Both dynamics are guided by the same geometric origin, allowing for a unified approach that allows for their prediction through a single construct. This geometric framework complements existing GB migration models by offering a unique predictive understanding of particle and defect movements at the microscopic level. Conversely, it does not inherently explain certain macroscopic processes, such as grain rotation that can accompany GB migration, which are more effectively described by other frameworks like the Cahn model[18,19]. Furthermore, our work represents a conceptual and practical extension of O-lattice theory[50], moving beyond its conventional structural applications[51–55] to address the microscopic dynamics underlying GB migration.

Inherent to its purely geometry-based nature, our general framework is applicable to a wide range of polycrystalline materials, including those with different lattice symmetries, irrespective of their scale, be it at the colloidal or the atomic level. The approach we have presented here is currently applied to two-dimensional materials, which are of great importance in their own right (for example, graphene). However, we believe that the geometric principles underlying our approach can also be extended to three-dimensional materials. Furthermore, while this work focuses on simple loop-shaped GBs, extending the approach to more complex GB networks—such as those found in real polycrystalline materials with multiple grains and triple junctions—represents an exciting future direction. In addition, exploring the possible connection between the transition points we identified and thermodynamic quantities, such as the free-energy landscape that particles explore during GB migration, offers a promising path for integrating these geometric insights with underlying thermodynamic driving forces. While these steps may be challenging, they could pave the way towards a deeper understanding of the microscopic mechanism of GB migration in three-dimensional materials and potentially enable the tailoring of their material properties.

Online content

Any methods, additional references, Nature Portfolio reporting summaries, source data, extended data, supplementary information, acknowledgements, peer review information; details of author contributions and competing interests; and statements of data and code availability are available at https://doi.org/10.1038/s41567-025-03165-4.

References

1. Howe, J. M. *Interfaces in Materials: Atomic Structure, Thermodynamics and Kinetics of Solid–Vapor, Solid-Liquid and Solid–Solid Interfaces* (Wiley, 1997).
2. Hall, E. O. The deformation and ageing of mild steel: III Discussion of results. *Proc. Phys. Soc. B* **64**, 747 (1951).
3. Petch, N. J. The cleavage strength of polycrystals. *J. Iron Steel Inst.* **174**, 25–28 (1953).
4. Wei, J. et al. Direct imaging of atomistic grain boundary migration. *Nat. Mater.* **20**, 951–955 (2021).
5. Wei, J., Feng, B., Tochigi, E., Shibata, N. & Ikuhara, Y. Direct imaging of the disconnection climb mediated point defects absorption by a grain boundary. *Nat. Commun.* **13**, 1455 (2022).
6. Sutton, A. P. & Vitek, V. On the structure of tilt grain boundaries in cubic metals I. Symmetrical tilt boundaries. *Philos. Trans. R. Soc. Lond. Ser. A* **309**, 1–36 (1983).
7. Brandon, D. G. The structure of high-angle grain boundaries. *Acta Metall.* **14**, 1479–1484 (1966).
8. Read, W. T. & Shockley, W. J. P. R. Dislocation models of crystal grain boundaries. *Phys. Rev.* **78**, 275 (1950).
9. Fang, Z. et al. Atomic-scale observation of dynamic grain boundary structural transformation during shear-mediated migration. *Sci. Adv.* **8**, eabn3785 (2022).
10. Tong, K. et al. Structural transition and migration of incoherent twin boundary in diamond. *Nature* **626**, 79–85 (2024).
11. Han, J., Thomas, S. L. & Srolovitz, D. J. Grain-boundary kinetics: a unified approach. *Prog. Mater. Sci.* **98**, 386–476 (2018).
12. Hirth, J. & Pond, R. Steps, dislocations and disconnections as interface defects relating to structure and phase transformations. *Acta Mater.* **44**, 4749–4763 (1996).
13. Khater, H., Serra, A., Pond, R. & Hirth, J. The disconnection mechanism of coupled migration and shear at grain boundaries. *Acta Mater.* **60**, 2007–2020 (2012).
14. Rajabzadeh, A., Legros, M., Combe, N., Mompiou, F. & Molodov, D. Evidence of grain boundary dislocation step motion associated to shear-coupled grain boundary migration. *Philos. Mag.* **93**, 1299–1316 (2013).
15. Rajabzadeh, A., Mompiou, F., Legros, M. & Combe, N. Elementary mechanisms of shear-coupled grain boundary migration. *Phys. Rev. Lett.* **110**, 265507 (2013).
16. Zhu, Q. et al. In situ atomistic observation of disconnection-mediated grain boundary migration. *Nat. Commun.* **10**, 156 (2019).
17. Anderson, P. M., Hirth, J. P. & Lothe, J. *Theory of Dislocations* (Cambridge Univ. Press, 2017).
18. Cahn, J. W. & Taylor, J. E. A unified approach to motion of grain boundaries, relative tangential translation along grain boundaries, and grain rotation. *Acta Mater.* **52**, 4887–4898 (2004).
19. Cahn, J. W., Mishin, Y. & Suzuki, A. Coupling grain boundary motion to shear deformation. *Acta Mater.* **54**, 4953–4975 (2006).
20. Babcock, S. & Balluffi, R. Grain boundary kinetics—ii. in situ observations of the role of grain boundary dislocations in high-angle boundary migration. *Acta Metall.* **37**, 2367–2376 (1989).
21. Zhang, L., Han, J., Xiang, Y. & Srolovitz, D. J. Equation of motion for a grain boundary. *Phys. Rev. Lett.* **119**, 246101 (2017).
22. Zhang, L., Han, J., Srolovitz, D. J. & Xiang, Y. Equation of motion for grain boundaries in polycrystals. *npj Comput. Mater.* **7**, 64 (2021).
23. Zhang, H. & Srolovitz, D. J. Simulation and analysis of the migration mechanism of Σ5 tilt grain boundaries in an fcc metal. *Acta Mater.* **54**, 623–633 (2006).
24. Zhang, H., Srolovitz, D. J., Douglas, J. F. & Warren, J. A. Characterization of atomic motion governing grain boundary migration. *Phys. Rev. B* **74**, 115404 (2006).
25. Crocker, J. C. & Grier, D. G. Methods of digital video microscopy for colloidal studies. *J. Colloid Interface Sci.* **179**, 298–310 (1996).
26. Weeks, E. R., Crocker, J. C., Levitt, A. C., Schofield, A. & Weitz, D. A. Three-dimensional direct imaging of structural relaxation near the colloidal glass transition. *Science* **287**, 627–631 (2000).
27. Gasser, U., Weeks, E. R., Schofield, A., Pusey, P. N. & Weitz, D. A. Real-space imaging of nucleation and growth in colloidal crystallization. *Science* **292**, 258–262 (2001).
28. Alsayed, A. M., Islam, M. F., Zhang, J., Collings, P. J. & Yodh, A. G. Premelting at defects within bulk colloidal crystals. *Science* **309**, 1207–1210 (2005).

29. Wang, Z., Wang, F., Peng, Y., Zheng, Z. & Han, Y. Imaging the homogeneous nucleation during the melting of superheated colloidal crystals. *Science* **338**, 87–90 (2012).
30. Kim, S., Svetlizky, I., Weitz, D. A. & Spaepen, F. Work hardening in colloidal crystals. *Nature* **630**, 648–653 (2024).
31. Wang, X., Li, B., Li, M. & Han, Y. Polymorphic crystalline wetting layers on crystal surfaces. *Nat. Phys.* **19**, 700–705 (2023).
32. Zhou, W. et al. Space-tiled colloidal crystals from dna-forced shape-complementary polyhedra pairing. *Science* **383**, 312–319 (2024).
33. Zang, S., Hauser, A. W., Paul, S., Hocky, G. M. & Sacanna, S. Enabling three-dimensional real-space analysis of ionic colloidal crystallization. *Nat. Mater.* **23**, 1131–1137 (2024).
34. Skinner, T. O. E., Aarts, D. G. A. L. & Dullens, R. P. A. Grain-boundary fluctuations in two-dimensional colloidal crystals. *Phys. Rev. Lett.* **105**, 168301 (2010).
35. Nagamanasa, K. H., Gokhale, S., Ganapathy, R. & Sood, A. K. Confined glassy dynamics at grain boundaries in colloidal crystals. *Proc. Natl Acad. Sci. USA* **108**, 11323–11326 (2011).
36. Li, W. et al. Shear-assisted grain coarsening in colloidal polycrystals. *Proc. Natl Acad. Sci. USA* **117**, 24055–24060 (2020).
37. Irvine, W. T. M., Hollingsworth, A. D., Grier, D. G. & Chaikin, P. M. Dislocation reactions, grain boundaries, and irreversibility in two-dimensional lattices using topological tweezers. *Proc. Natl Acad. Sci. USA* **110**, 15544–15548 (2013).
38. Cash, C. E. et al. Local melting attracts grain boundaries in colloidal polycrystals. *Phys. Rev. Lett.* **120**, 018002 (2018).
39. Lavergne, F. A., Curran, A., Aarts, D. G. A. L. & Dullens, R. P. A. Dislocation-controlled formation and kinetics of grain boundary loops in two-dimensional crystals. *Proc. Natl Acad. Sci. USA* **115**, 6922–6927 (2018).
40. Lavergne, F. A., Curran, A., Aarts, D. G. A. L. & Dullens, R. P. A. Shrinkage mechanisms of grain boundary loops in two-dimensional colloidal crystals. *Eur. Phys. J. B* **92**, 142 (2019).
41. Barth, A. R. et al. Grain splitting is a mechanism for grain coarsening in colloidal polycrystals. *Phys. Rev. E* **104**, L052601 (2021).
42. Thorneywork, A. L., Abbott, J. L., Aarts, D. G. A. L. & Dullens, R. P. A. Two-dimensional melting of colloidal hard spheres. *Phys. Rev. Lett.* **118**, 158001 (2017).
43. Gottstein, G. & Shvindlerman, L. S. *Grain Boundary Migration in Metals: Thermodynamics, Kinetics, Applications* (CRC Press, 2009).
44. Humphreys, F. J. & Hatherly, M. *Recrystallization and Related Annealing Phenomena* (Elsevier, 2012).
45. Ranganathan, S. On the geometry of coincidence-site lattices. *Acta Crystallogr.* **21**, 197–199 (1966).
46. Race, C. P., Hadian, R., von Pezold, J., Grabowski, B. & Neugebauer, J. Mechanisms and kinetics of the migration of grain boundaries containing extended defects. *Phys. Rev. B* **92**, 174115 (2015).
47. Chesser, I., Holm, E. & Runnels, B. Optimal transportation of grain boundaries: a forward model for predicting migration mechanisms. *Acta Mater.* **210**, 116823 (2021).
48. Chesser, I., Runnels, B. & Holm, E. A taxonomy of grain boundary migration mechanisms via displacement texture characterization. *Acta Mater.* **222**, 117425 (2022).
49. Hull, D. & Bacon, D. J. *Introduction to Dislocations* (Butterworth-Heinemann, 2001).
50. Bollmann, W. *Crystal Defects and Crystalline Interfaces* (Springer, 1970).
51. Bollmann, W. O-lattice calculation of an fcc–bcc interface. *Phys. Status Solidi A* **21**, 543–550 (1974).
52. Duly, D., Zhang, W.-Z. & Audier, M. High-resolution electron microscopy observations of the interface structure of continuous precipitates in a Mg–Al alloy and interpretation with the O-lattice theory. *Philos. Mag. A* **71**, 187–204 (1995).
53. Tsurekawa, S., Morita, K., Nakashima, H. & Yoshinaga, H. Geometric structures of grain boundaries expected from the O-lattice theory compared with high-resolution transmission electron microscope images. *Mater. Trans.* **38**, 393–400 (1997).
54. Zhou, J. et al. High-resolution electron microscopy observations of continuous precipitates with pitsch-schrader orientation relationship in an Mg–Al based alloy and interpretation with the O-lattice theory. *Micron* **40**, 906–910 (2009).
55. Cherkashin, N., Kononchuk, O., Reboh, S. & Hÿtch, M. Application of the O-lattice theory for the reconstruction of the high-angle near 90° tilt Si (110)/(001) boundary created by wafer bonding. *Acta Mater.* **60**, 1161–1173 (2012).
56. Sanz, E. & Marenduzzo, D. Dynamic Monte Carlo versus Brownian dynamics: a comparison for self-diffusion and crystallization in colloidal fluids. *J. Chem. Phys.* **132**, 194102 (2010).
57. Baruffi, C., Finel, A., Le Bouar, Y., Bacroix, B. & Salman, O. U. Overdamped Langevin dynamics simulations of grain boundary motion. *Mater. Theory* **3**, 1–26 (2019).
58. Camerin, F. et al. Disentangling the effects of curvature and misorientation on the shrinkage behavior of loop-shaped grain boundaries. *Phys. Rev. Lett.* **135**, 178202 (2025).
59. van der Meer, B., Qi, W., Sprakel, J., Filion, L. & Dijkstra, M. Dynamical heterogeneities and defects in two-dimensional soft colloidal crystals. *Soft Matter* **11**, 9385–9392 (2015).
60. Zhang, H., Srolovitz, D. J., Douglas, J. F. & Warren, J. A. Grain boundaries exhibit the dynamics of glass-forming liquids. *Proc. Natl Acad. Sci. USA* **106**, 7735–7740 (2009).

Methods

Experimental details

Colloidal system. We create two-dimensional monolayer colloidal crystals using melamine formaldehyde spheres (microParticles) with a diameter of $\sigma = 2.82$ µm. The spheres are suspended in an ethanol/water mixture (20/80;v/v%) to produce hard-sphere interactions[42], and then loaded into a 200-µm-thick quartz cell (Hellma Analytics). The high density difference between the spheres and solvent causes the spheres to rapidly settle to the bottom of the container, resulting in a two-dimensional system with negligible out-of-plane motion. By selecting a high packing fraction ($\phi \approx 0.74$–0.76), we formed two-dimensional crystals, which were left to coarsen for about a week to create large crystal domains that span the entire field of view.

Creation and microscopy of loop-shaped GBs. We use a holographic optical tweezing technique similar to the one described in ref. 39 to generate loop-shaped GBs with a typical diameter of ~70 lattice spacings. A defocused optical vortex was generated using a spatial light modulator (Meadowlark) to rotate a circular patch of crystal within the two-dimensional colloidal crystal while the vortex was active. Upon reaching the desired misorientation, the vortex was deactivated and the shrinkage of the domain proceeded freely without external forces. The loop-shaped GBs were created within a large single domain area to keep them isolated from other GBs in the sample. Bright field video-microscopy was utilized to monitor the GB shrinkage process at the single-particle level, and particle positions were determined using a standard particle tracking algorithm[25].

Simulation details

Dynamic Monte Carlo simulations. We use the dMC method[56] to simulate hard disks in the canonical ensemble. In this ensemble, the temperature T, the number of particles N and the area A of the simulation box are kept constant, thus fixing the particle number density $\rho = N/A$. The system is evolved through small MC steps at a high acceptance rate, which has been shown to ensure an accurate Brownian dynamics[56]. More specifically, during an MC step, a particle is chosen at random and a trial move is generated by translating it a random distance in the range of $[-\delta_t, \delta_t]$ along each Cartesian axis. Trial moves that result in an overlap with nearby particles are rejected. Using $\delta_t \approx 0.005\sigma$ a high acceptance rate is achieved (>0.9).

Creation of starting configurations. All dMC simulations were started from starting configurations that were generated by first creating a map of all possible dislocations sites (Fig. 4e–g). A loop-shaped GB was initialized by choosing a loop-shaped path of dislocations sites and placing particles inside (outside) this loop on lattice sites of the rotated (host) crystal. Particles located at the chosen dislocation sites do not belong to either grain and are placed at the centre of their O-cell. A few examples of the starting configuration obtained using this procedure are shown in Extended Data Fig. 4. Here, each potential dislocation site is plotted as a black line with its orientation representing the line that connects the 7 and 5 defects. The selected dislocation sites are highlighted in yellow. The generated configurations may exhibit occasional hard-particle overlaps, which are simply rectified by executing a few dMC sweeps with interactions simulating a strongly repulsive core. Importantly, this construction method leads to a uniform spacing between GB dislocations, and ensures that, irrespective of the initial GB loop size chosen, the total number of lattice sites matches the number of particles. As a result, complete shrinkage of the GB loop leads to the formation of a defect-free single crystal. Note that our system size is substantially larger than the region shown in Extended Data Fig. 4 to minimize finite-size effects.

Biasing of the misorientation. To study the effect of grain rotation, we perform dMC simulations in which the misorientation was biased via an external potential. This involves keeping track of the GB misorientation and biasing its trajectory such that throughout the skrinkage process $\theta(t) \approx \theta_0$ with θ_0 the initial GB misorientation. To monitor the GB misorientation, we first calculate the bond-orientational order parameter of each particle j as given by:

$$\psi_{6,j} = \frac{1}{N_j}\sum_{k=1}^{N_j} e^{i6\Delta\theta_{jk}}, \tag{4}$$

where N_j is the number of nearest neighbours of particle j as determined by a Voronoi construction, and $\Delta\theta_{jk}$ is the angle formed between a fixed axis and the vector connecting particle j and its nearest neighbours k. The local orientation $\varphi_{6,j}$ of each particle j was subsequently calculated using

$$\varphi_{6,j} = \arg(\psi_{6,j})/6. \tag{5}$$

To distinguish between particles belonging to the rotated and host crystals, we categorize all particles whose local orientation is closer to that of the rotated grain as 'rotated-like'. Next, we calculate the orientation of the rotated crystal φ_{rotated} by identifying the largest cluster of these rotated-like particles and calculating its mean orientation. Likewise, the orientation of the host crystal φ_{host} can be determined, which was observed to remain constant throughout our simulations. The GB misorientation associated with the particle positions $\mathbf{r}^N$ is now given by

$$\theta(\mathbf{r}^N) = \min(|\varphi_{\text{host}} - \varphi_{\text{rotated}}|, \frac{\pi}{3} - |\varphi_{\text{host}} - \varphi_{\text{rotated}}|). \tag{6}$$

To prevent grain rotation, we introduce a harmonic biasing potential given by

$$U_{\text{bias}} = \frac{\lambda}{2}(\theta(\mathbf{r}^N) - \theta_0)^2 \tag{7}$$

with λ controlling the width of the biasing potential centred around the desired misorientation, which is the initial misorientation θ_0. As the computation of U_{bias} is computationally demanding, it is more practical to refrain from calculating it for each individual dMC step. Instead, a brief, unbiased dMC run of roughly 10^2 dMC sweeps is performed. Subsequently, biasing is imposed by rejecting or accepting this trial sequence according to:

$$\text{acc}(\text{old} \to \text{new}) = \min(1, e^{-\beta\Delta U_{\text{bias}}}), \tag{8}$$

where $\beta = 1/k_B T$ with k_B the Boltzmann constant and T the temperature. Using $\beta\lambda \approx 1{,}000$, GB shrinkage proceeds without any simultaneous grain rotation. More specifically, during the shrinkage process the misorientation remains constant, with typical fluctuations around θ_0 on the order of ±0.1° (Extended Data Fig. 5).

Interaction details of the systems with continuous, soft and attractive interactions. The geometric nature of the framework allows us to straightforwardly apply it to systems with diverse interaction types. To assess the robustness of our predictions against changes in interparticle interaction, we investigated three additional two-dimensional systems for a range of dimensionless number densities $\rho\sigma^2$ (Extended Data Fig. 6). In all dMC simulations for these systems, we applied a biasing potential to ensure a constant misorientation during each run.

The first system is composed of Weeks–Chandler–Andersen particles modelling short-ranged, yet continuous, repulsive interactions given by

$$\beta U(r) = 4\beta\epsilon_{\text{WCA}}\left(\left(\frac{\sigma}{r}\right)^{12} - \left(\frac{\sigma}{r}\right)^{6} + \frac{1}{4}\right) \tag{9}$$

with $r = |\mathbf{r}_i - \mathbf{r}_j|$ the centre-of-mass distance between particle i and j, σ the particle diameter, $r_{cut} = 2^{1/6}\sigma$ the interaction cut-off radius and $\beta\epsilon_{WCA} = 200$ the dimensionless energy scale.

The second system consists of Yukawa particles exhibiting substantially longer-ranged soft repulsive interactions given by

$$\beta U(r) = \beta\epsilon_Y \frac{\exp(-\kappa(r-\sigma))}{r/\sigma} \tag{10}$$

with the dimensionless Debye screening length $\kappa\sigma = 2.25$, and the contact value $\beta\epsilon_Y = 235$ (ref. 59). The interactions were truncated and shifted at $r_{cut} = 4.0\sigma$. We note that at a low misorientation $\theta_0 \approx 9°$, we did not observe annihilation of the GB loop, precluding a comparison between predicted and observed dynamics in this specific case.

Finally, we also investigated a system with attractive interactions using the well-known Lennard–Jones potential:

$$\beta U(r) = 4\beta\epsilon_{LJ}\left(\left(\frac{\sigma}{r}\right)^{12} - \left(\frac{\sigma}{r}\right)^{6}\right). \tag{11}$$

Here the attraction strength was set to $\beta\epsilon_{LJ} = 2.0$. The interactions were truncated and shifted at $r_{cut} = 2.5\sigma$.

Analysis details

Dislocation identification. In our two-dimensional hexagonal crystals, dislocations appear as pairs of five- and sevenfold coordinated particles that decorate the GB line with a dislocation spacing of approximately a/θ, where a is the lattice spacing. Hence, for low misorientations, dislocations are clearly distinguishable from each other as isolated pairs of 5–7 defects (see, for example, Fig. 1e), making their identification straightforward. However, at higher misorientations, dislocations do not appear as isolated pairs of 5–7 defects but tend to form extended chains, resembling defect sequences like 5–7–5–7–5–7 along the GB (Extended Data Fig. 7a). This complicates the identification of individual dislocations. To address this issue, we first identify all chains of defects in our system. Subsequently, within a given chain we identify the starting fivefold defect in the chain, characterized by having only a single sevenfold neighbour. The first dislocation in the chain is now recognized as this pair of 5 and 7 defects. Once this dislocation is attributed, the procedure proceeds by pairing the next fivefold defect in the sequence with its corresponding sevenfold neighbour. This process, where dislocations are attributed in a step-by-step manner, is illustrated in Extended Data Fig. 7b, and continues until all dislocations within the chain have been identified. In practice, we execute this procedure starting from both ends of the chain, which at the tail of the chain involves identifying the ending sevenfold defect that has only one fivefold neighbour (Extended Data Fig. 7b).

Aligning the particle displacement map. Using our O-cell construction, we generate a map of predicted particle displacements derived from the separation vector between the two lattice sites encapsulated in each 'filled' O-cell. To compare these predicted displacements with the particle movement observed in experiments and simulations, it is crucial to align the origin of the predicted displacement map with that of the observed displacements. In our dMC simulations, the origin of the displacement map consistently coincided with the grain's centre of rotation. However, this was not observed in our experiments. While our simulations feature a continuous GB with a clearly defined, single origin, experimental GBs often show local disruptions owing to defects beyond simple GB dislocations. This means that different parts of an experimental GB can have slightly offset 'origins'. This behaviour is commonly seen in CSL boundaries, where disconnections induce a shift of the CSL sites (see for example, ref. 11). As a result, choosing an origin that aligns the predicted and observed displacements in one region of the GB typically leads to mismatches in other areas. This suggests that a large experimental GB loop may not possess necessarily a single, global O-lattice origin. Nevertheless, we find that locally there is always a well-defined origin. By aligning regions around locally immobile particles, we observe excellent agreement between the predicted and experimental particle displacements. This local consistency is why we find excellent agreement between the predicted and observed particle displacements, even when the overall experimental GB lacks a single, global origin.

Quantifying the agreement between predicted and observed particle displacements. To systematically investigate the agreement between the predicted and observed particle displacements, we use dMC simulations and monitor the fraction of particles that displace as predicted by our O-cell approach. The simulations were started from GB-loop configurations with a diameter of approximately ~50 lattice spacings (see, for example, Extended Data Fig. 4), which were created through our GB construction method. During the GB shrinkage process, particles in the rotated crystal displace from lattice sites of the rotated crystal to lattice sites of the host crystal. Hence, for each particle, its displacement can be tracked by identifying its original lattice site within the rotated crystal and its destination lattice site within the host crystal. In practice, we track this displacement for each particle by establishing a point-to-point mapping using the following process. First, for a snapshot captured at the start of the simulation, we determine the particle's original lattice site by finding its closest corresponding lattice site in the rotated crystal domain. Next, for a snapshot taken at the end of the simulation, when the GB loop has annihilated, we determine the particle's final lattice site by finding its closest corresponding lattice site in the host crystal domain. This point-to-point analysis defines the observed particle displacement mapping. This obtained mapping between specific lattice sites can then be directly compared with the mapping predicted by our O-cell approach. For each particle displacement, our criterion for agreement is an exact match between these two mappings; no subjective cut-off or tolerance is applied. Note that we restrict our analysis to GB misorientations where no incoherent O-cells occur, as particles in incoherent O-cells have a 'free choice' which neighbouring filled O-cell to occupy, setting off a chain of non-deterministic displacements. Furthermore, it is worth noting that we only consider displacements while the grain size is larger than the plastic-to-elastic transition[39], as it has been demonstrated that GB shrinkage proceeds through a distinct mechanism for small grain sizes.

Data availability

The data contained in the plots within this paper and other datasets examined in this study can be obtained from the corresponding author upon reasonable request.

Code availability

The code to generate the geometric O-lattice constructions introduced in this study are available as a Jupyter Notebook at https://github.com/Dullens-Lab/o_lattice_constructions.

Acknowledgements

B.v.d.M. acknowledges funding from the Netherlands Organisation for Scientific Research (NWO) through a Rubicon grant (NWO-Rubicon Grant No. 019.191EN.011) and Veni grant (Veni Grant No. VI.Veni.212.138). R.P.A.D. acknowledges financial support from the European Research Council (Consolidator Grant No. 724834-OMCIDC).

Author contributions

Conceptualization: B.v.d.M., M.G.B. and R.P.A.D. Formal analysis: B.v.d.M., M.G.B. and F.A.L. Funding acquisition: B.v.d.M. and R.P.A.D. Investigation: B.v.d.M. and M.G.B. Methodology: B.v.d.M., M.G.B., F.A.L.

and A.C. Supervision: M.D. and R.P.A.D. Writing—original draft: B.v.d.M. and R.P.A.D. Writing—review and editing: all authors.

Competing interests
The authors declare no competing interests.

Additional information
Extended data is available for this paper at https://doi.org/10.1038/s41567-025-03165-4.

Correspondence and requests for materials should be addressed to Roel P. A. Dullens.

Peer review information *Nature Physics* thanks the anonymous reviewers for their contribution to the peer review of this work.

https://doi.org/10.1038/s41567-025-03165-4

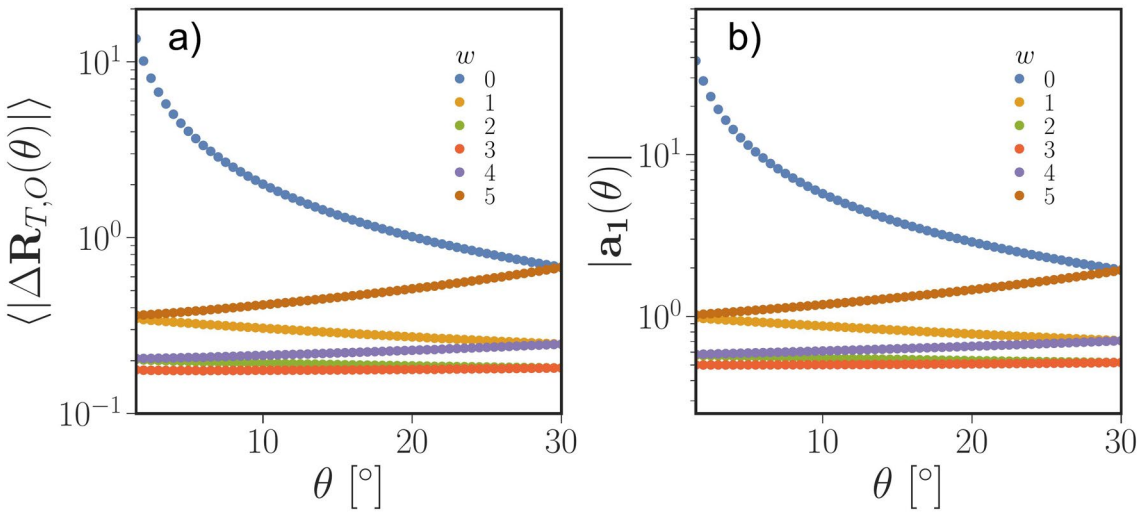

Extended Data Fig. 1 | Effect of w on the resulting O-lattice. (**a**) The calculated average distance between a lattice site and its nearest O-lattice site $\langle|\Delta\mathbf{R}_{T,O}|\rangle$, and (**b**) the O-lattice spacing, that is the length of the O-lattice vector $|\mathbf{a}_1|$, both as a function of the misorientation θ for all values of w. Note that panel (**a**) is equivalent to Fig. 2(d) in the main text.

https://doi.org/10.1038/s41567-025-03165-4

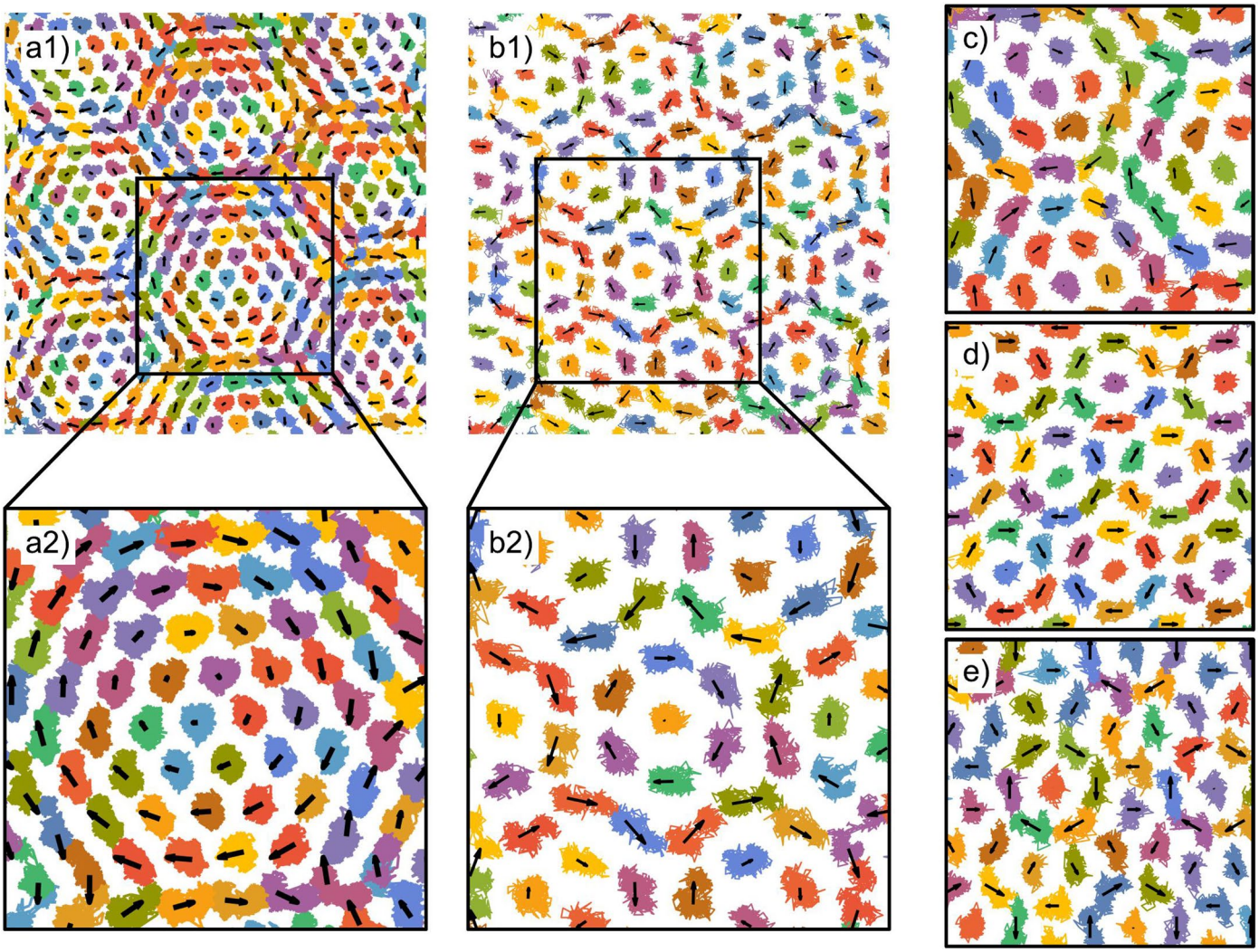

Extended Data Fig. 2 | Predicting the particle dynamics underlying GB migration through O-cell construction. (**a**-**e**) Particle trajectories as observed in experiments with superimposed the particle displacements as predicted by our O-cell approach (black arrows) for (**a**) $\theta = 9^{\circ}$, (**b**) $\theta = 18^{\circ}$, and for (near)-CSL misorientations (**c**) $\theta = 13^{\circ}$, (**d**) $\theta = 22^{\circ}$, and (**e**) $\theta = 28^{\circ}$, corresponding to $\Sigma 19$, $\Sigma 7$, and $\Sigma 13$ GBs, respectively. Note that panels (**a**,**b**) are equivalent to Fig. 3(a,b) in the main text.

https://doi.org/10.1038/s41567-025-03165-4

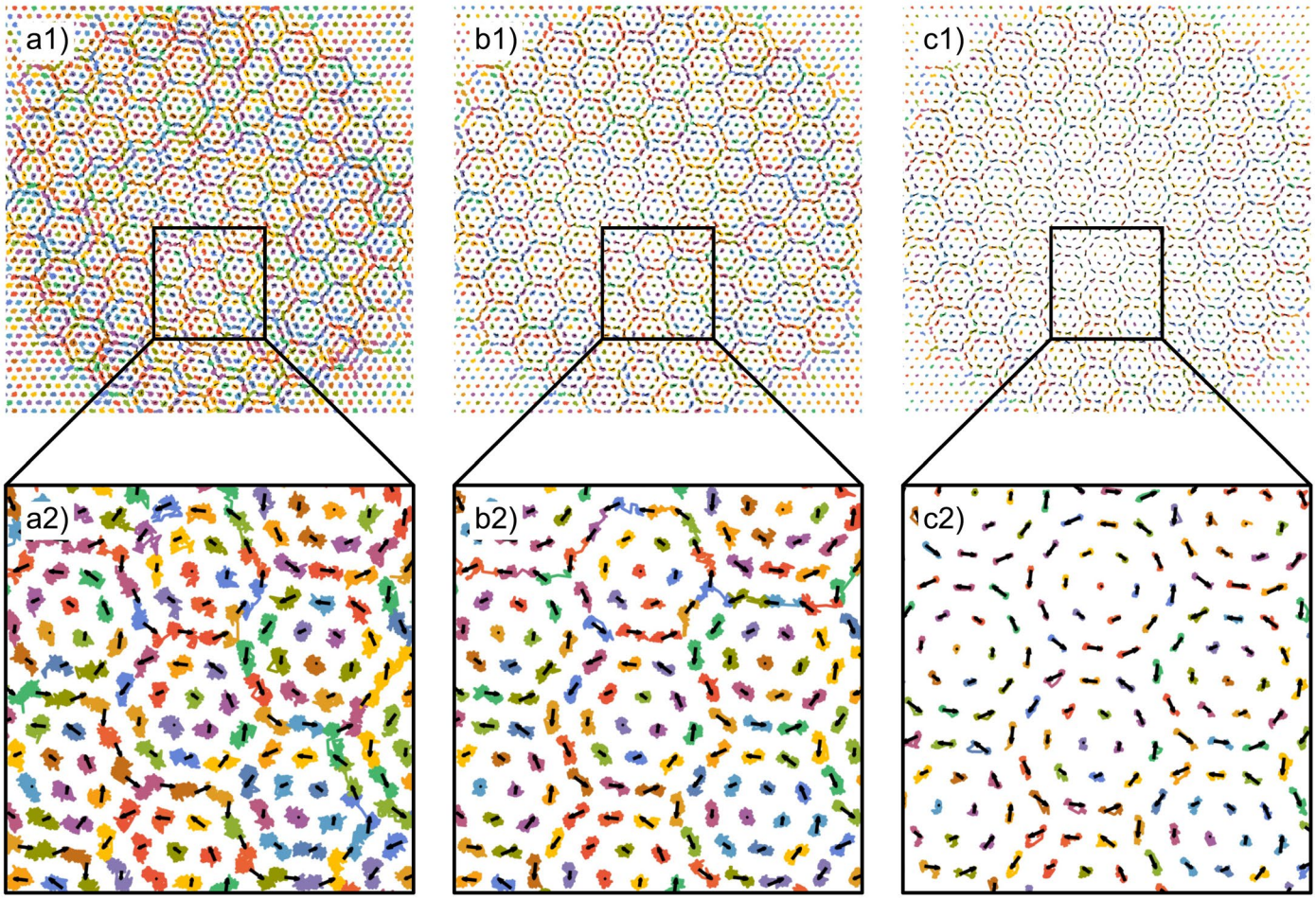

Extended Data Fig. 3 | Effect of thermal fluctuations on the particle dynamics during GB migration as observed in dMC simulations. (**a**-**c**) Particle trajectories with superimposed the particle displacements as predicted by our O-cell approach (black arrows) for an misorientation of $\theta = 13.2^{\circ}$ for a packing fraction (**a**) $\phi = 0.78$, (**b**) $\phi = 0.82$, and (**c**) $\phi = 0.84$, respectively.

https://doi.org/10.1038/s41567-025-03165-4

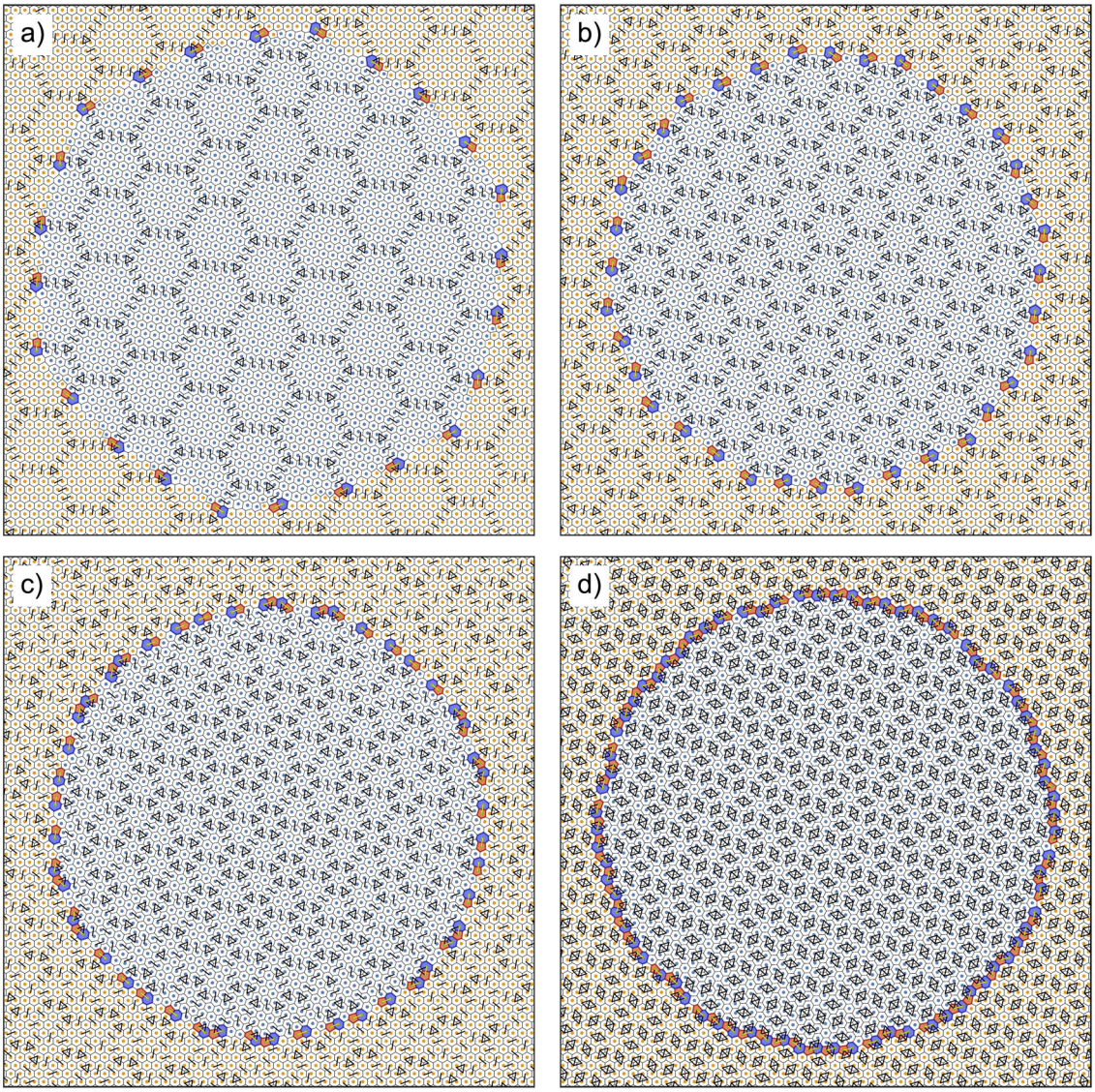

Extended Data Fig. 4 | Starting configurations created using the map of possible dislocation sites. Starting configurations for (**a**) $\theta = 9^{\circ}$, (**b**) $\theta = 13^{\circ}$, (**c**) $\theta = 18^{\circ}$, and (**d**) $\theta = 28^{\circ}$. Here, each potential dislocation site is plotted as a black line with its orientation given by the line that connects the 7- and 5-defect. A loop-shaped GB is constructed by selecting a circular path of dislocation sites (lines highlighted in yellow) and placing particles inside (outside) this loop on lattice sites of the blue (orange) crystal. Dislocations appear as pairs of 7- and 5-fold coordinated defects upon Voronoi construction (highlighted as blue and red cells).

https://doi.org/10.1038/s41567-025-03165-4

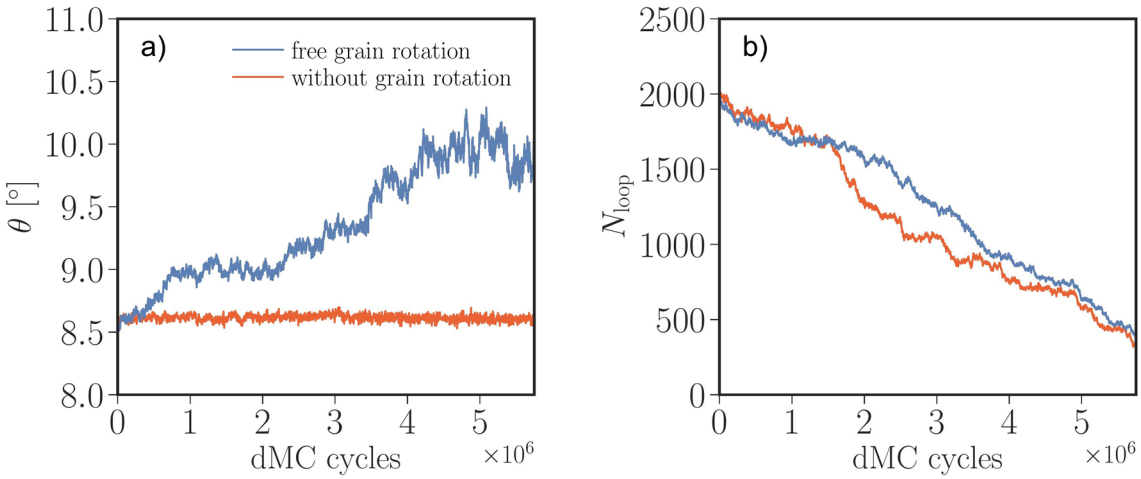

Extended Data Fig. 5 | Effect of external biasing on the misorientation θ during GB loop shrinkage for single simulation runs. (**a**) Without external biasing, grain rotation occurs freely during the shrinkage process (blue line). Upon introducing a harmonic biasing potential the misorientation θ remains virtually constant over time (red line). (**b**) The corresponding size evolution of the GB loop, monitored through the number of particles N_{loop} that comprise the rotated crystal domain. Packing fraction: $\phi = 0.84$.

https://doi.org/10.1038/s41567-025-03165-4

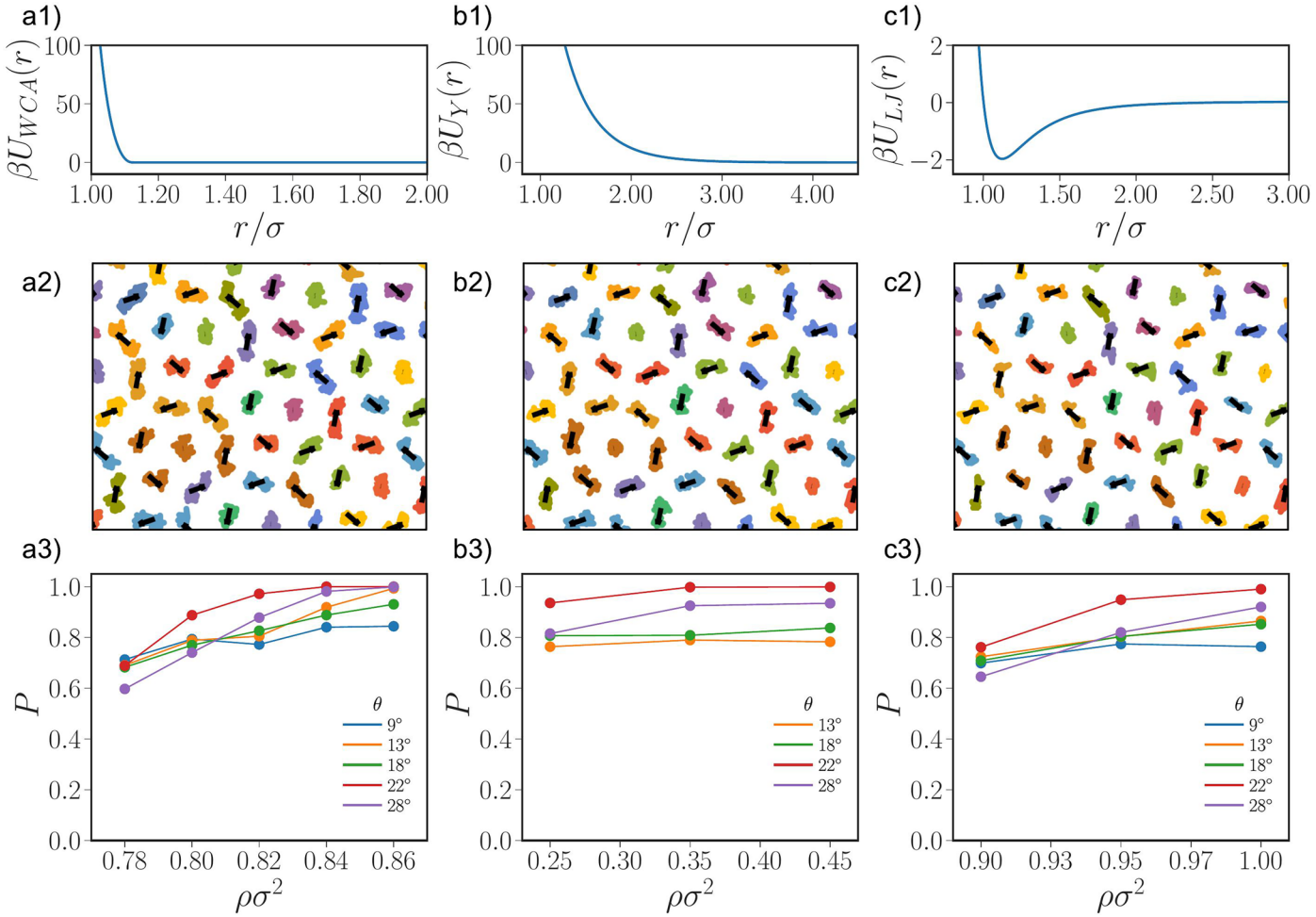

Extended Data Fig. 6 | Assessing the robustness of our geometric predictions for particle dynamics across a diverse range of interactions. (**a1**, **b1**, **c1**) Interaction potential for the Weeks-Chandler-Andersen, Yukawa, and Lennard-Jones system, respectively. (**a2**, **b2**, **c2**) Particle trajectories with superimposed the particle displacements as predicted by our O-cell approach (black arrows) for a misorientation of $\theta = 21.8^{\circ}$ for (a2) the Weeks-Chandler-Andersen system at $\rho\sigma^2 = 0.84$, (b2) the Yukawa system at $\rho\sigma^2 = 0.35$, and (c2) the Lennard-Jones system at $\rho\sigma^2 = 0.35$. (**a3**, **b3**, **c3**) The fraction of particles, P, that displace as predicted for various misorientations θ, plotted as a function of the particle number density $\rho\sigma^2$ for the three systems, respectively. The error bars for each state point ($N = 4$) are on the order of the symbol size or smaller and are omitted to retain a clear presentation of the data. As the particle number density $\rho\sigma^2$ increases, the agreement with the geometric predictions becomes stronger. Throughout all dMC simulations, the misorientation was kept constant using an external biasing potential.

https://doi.org/10.1038/s41567-025-03165-4

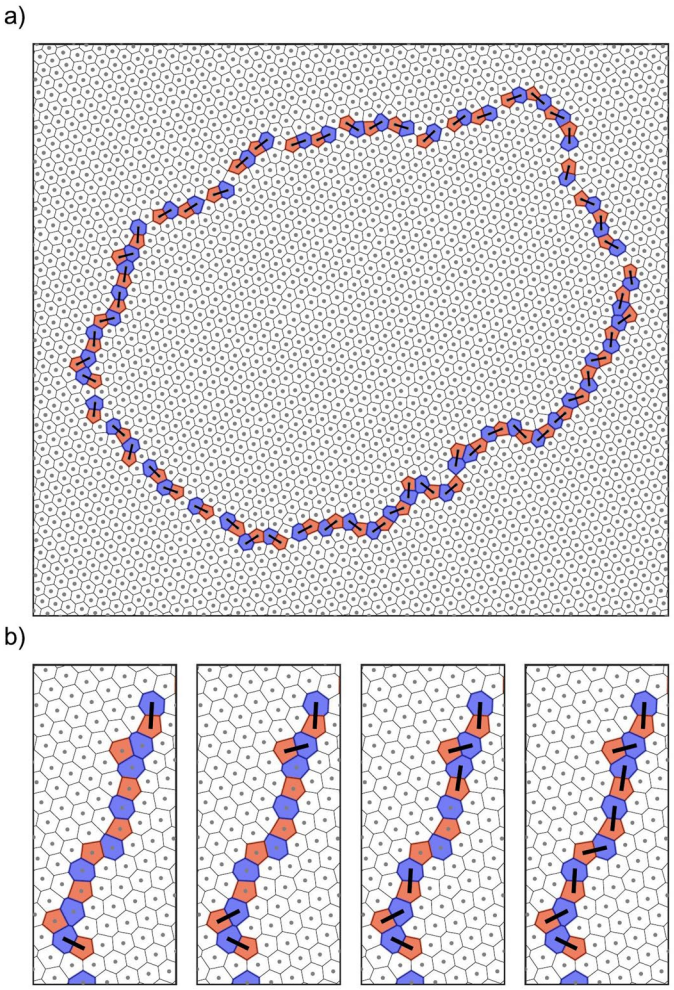

Extended Data Fig. 7 | Dislocation identification for a misorientation of $\theta_0 = 28^\circ$ in experiments. (**a**) Identification of dislocations that comprise the high-angle GB loop. Here, identified dislocations are highlighted with a superimposed black line connecting their 7- and 5-defect defects. (**b**) Sequential series depicting the same dislocation chain, demonstrating the step-by-step process of dissecting a chain into individual dislocations. The initial step involves identifying the head and tail dislocations, followed by successive steps to pinpoint the subsequent dislocations in the chain until all dislocations are identified.